Soft Matter

PAPER

View Article Online
View Journal | View Issue

Cite this: *Soft Matter*, 2021, **17**, 1912

Interplay between cooperativity of intercellular receptor–ligand binding and coalescence of nanoscale lipid clusters in adhering membranes†

Long Li,[a] Jinglei Hu, *[b] Xinghua Shi, [c] Bartosz Różycki *[d] and Fan Song *[ae]

Received 26th October 2020,
Accepted 17th December 2020

DOI: 10.1039/d0sm01904f

rsc.li/soft-matter-journal

Adhesion of biological cells is mediated by the specific binding of receptors and ligands which are typically large proteins spanning through the plasma membranes of the contacting cells. The receptors and ligands can exhibit affinity for nanoscale lipid clusters that form within the plasma membrane. A central question is how these nanoscale lipid clusters physically affect and respond to the receptor–ligand binding during cell adhesion. Within the framework of classical statistical mechanics we find that the receptor–ligand binding reduces the threshold energy for lipid clusters to coalesce into mesoscale domains by up to ~50%, and that the formation of these domains induces significant cooperativity of the receptor–ligand binding. The interplay between the receptor–ligand binding cooperativity and the lipid domain formation manifests acute sensitivity of the membrane system to changes in control parameters. This sensitivity can be crucial in cell signaling and immune responses.

1 Introduction

Adhesion of cell membranes is essential for many biological processes (such as tissue formation, signal transduction, and immune responses) and results from the specific binding of membrane-anchored receptor and ligand proteins, as illustrated in Fig. 1a. This receptor–ligand binding is restricted to the two-dimensional (2D) membrane interface. A central quantity characterizing the binding is the equilibrium constant $K = [RL]/([R][L])$ that involves the area concentrations of receptor–ligand complexes [RL], free receptors [R], and free ligands [L]. Various techniques have been used to measure K.[1–8] However, in contrast to protein binding in solution, the receptor–ligand binding at the membrane interface can be determined not only by specific protein–protein interactions but also by physical properties of the membranes.[9–12] Moreover, if the binding is a cooperative process, the value of K alone is insufficient to quantify the binding equilibrium.

Cooperative binding of biomolecules is a common phenomenon. Prominent examples include the cooperative binding of oxygen molecules to hemoglobin[13] and the cooperative binding of calcium ions to calmodulin.[14] Theoretical modeling,[15–18] computer simulations[9,17,18] and recent experiments[10,11] have shown that the binding of membrane adhesion proteins can be a cooperative process due to membrane-mediated interactions. A physical picture is that the formation of the receptor–ligand complexes suppresses fluctuations in the distance between the two membranes which, in turn, facilitates formation of additional receptor–ligand complexes. The feedback between the suppression of membrane fluctuations and the formation of receptor–ligand complexes gives rise to cooperativity in the process of receptor–ligand binding, which can be quantified by the Hill coefficient n_H defined as the slope of binding curves in the Hill plot of $\log([RL]/[R])$ *versus* $\log([L])$. For flexible membranes and typical concentrations of the receptor and ligand proteins in cell adhesion zones, the membrane-mediated binding cooperativity is reflected in a modified law of mass action $[RL] \propto [R]^2[L]^2$.[15,29]

The membrane-mediated binding cooperativity has been studied so far in model membranes with rather uniform lipid distributions. Cell membranes, however, are multicomponent and heterogeneous supramolecular systems, containing the so-called lipid rafts, which are fluctuating nanoscale molecular clusters enriched in sphingolipids and cholesterol.[19–24] Lipid

[a] *State Key Laboratory of Nonlinear Mechanics and Beijing Key Laboratory of Engineered Construction and Mechanobiology, Institute of Mechanics, Chinese Academy of Sciences, Beijing, China. E-mail: songf@lnm.imech.ac.cn; Fax: +86-10-8254-3977; Tel: +86-10-8254-3691*

[b] *Kuang Yaming Honors School and Institute for Brain Sciences, Nanjing University, Nanjing, China. E-mail: hujinglei@nju.edu.cn; Fax: +86-25-8968-1298; Tel: +86-25-8968-1298*

[c] *National Center for Nanoscience and Technology of China, Beijing, China*

[d] *Institute of Physics, Polish Academy of Sciences, Al. Lotników 32/46, Warsaw, Poland. E-mail: rozycki@ifpan.edu.pl; Fax: +48-22-843-0926; Tel: +48-22-116-3265*

[e] *School of Engineering Science, University of Chinese Academy of Sciences, Beijing, China*

† Electronic supplementary information (ESI) available. See DOI: 10.1039/d0sm01904f

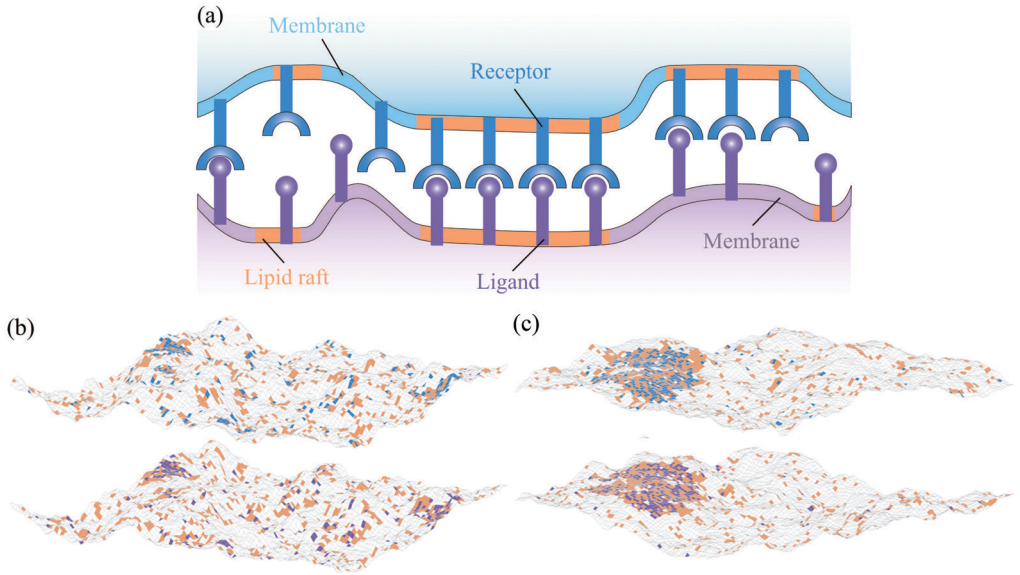

Fig. 1 Illustration of the system under study. (a) Cartoon of two membranes that adhere *via* receptor–ligand binding. Lipid rafts are shown in orange, membrane-anchored receptors in blue, and membrane-anchored ligands in purple. (b) and (c) Two snapshots from Monte Carlo simulations of adhering membranes. The roughness of the adhering membranes reflects thermal fluctuations. Lipid rafts, receptors and ligands are indicated by square patches with the same color code as in panel (a). Each receptor or ligand occupies a single membrane patch and exhibits weak affinity for lipid rafts, as reflected by colocalization of the blue and purple patches within the orange patches. One receptor only binds to one ligand if they are opposite each other and if their distance is within the binding range. Both the adhesion proteins and lipid rafts diffuse laterally within the membranes. The snapshot in panel (b) illustrates a homogeneous state in which many small rafts are distributed more-or-less uniformly in the membranes. The snapshot in panel (c) illustrates a phase-separated state in which lipid rafts form stable mesoscale domains.

rafts have larger rigidity and hydrophobic thickness than the membrane matrix. The surface area and length of protein transmembrane domains as well as protein palmitoylation are the major factors determining the affinity of membrane proteins for lipid rafts.[25] Interestingly, lipid rafts have been observed to associate with adhesion receptors of immune system cells.[26–30] For example, recent studies provide evidence for the role of lipid rafts in B-cell receptor signaling and a plausible mechanism of B-cell receptor activation *via* receptor clustering.[31] Many important questions about lipid rafts remain,[22] *e.g.*, how the intercellular receptor–ligand binding influences the spatial distribution of lipid rafts and how, in turn, the properties of lipid rafts affect the binding affinity and cooperativity.

We use methods of classical statistical mechanics and computational physics to study systems of adhering membranes in which the receptor and ligand proteins have affinity for lipid rafts, as illustrated in Fig. 1a. To capture the relevant physics of such systems, we take into account several generic phenomena, including (i) 2D diffusion of the membrane-anchored receptor and ligand proteins, (ii) formation and dissociation of the receptor–ligand complexes, (iii) diffusion, coalescence and fission of lipid rafts, (iv) elastic deformations of the two membranes, (v) the difference in bending rigidities between the membrane matrix and lipid rafts, and (vi) the affinity of the receptor and ligand proteins for lipid rafts. We find that, in a biologically relevant range of model parameters, the receptor–ligand binding can stabilize lipid rafts and make them to coalesce and grow into mesoscopic domains. As the domains are formed, the values of both K and n_{H} increase abruptly, indicating a significant amplification of both the affinity and cooperativity of the receptor–ligand binding. The interplay between the domain formation and the binding amplification manifests acute sensitivity of the system to small changes in such molecular factors as the lipid composition of the membranes or the binding sites of the receptor and ligand proteins. This sensitivity can be crucial in cell signaling, especially in the context of immune system cells.

2 Model and methods

The adhesion of cell membranes involves multiple length scales ranging from Angstroms (specific binding of the receptor and ligand proteins) to micrometers (lateral size of a typical adhesion zone). To deal with such complexity, it is necessary to use simplified theoretical models and apply suitable approximations. We employ a modeling approach that has been widely used to study both the equilibrium properties[32–34] and the dynamics[35,36] of biomembranes. It is based on representing membranes by 2D surfaces with the elastic energy given by the Helfrich Hamiltonian,[37] and then discretizing these surfaces into 'patches' of linear size a larger than the membrane thickness (Fig. 1b). The shapes of two apposing membranes can be described in the Monge parameterization by their local heights h_i^{o} from a reference plane, where the superscript $\mathrm{o} = +, -$ distinguishes the upper and lower membranes and the index $i = (i_x, i_y)$ labels sites on a 2D square lattice. To prevent the two membranes from overlapping, one considers only configurations with $h_i^{+} > h_i^{-}$. For two tensionless membranes that have no

spontaneous curvature, the bending energy is then given by[32,33]

$$\mathscr{H}_{\mathrm{me}} = \sum_{\mathrm{o}=+,-} \sum_i \frac{\kappa_i^{\mathrm{o}}}{2a^2} \left(\Delta_{\mathrm{d}} h_i^{\mathrm{o}}\right)^2 \quad (1)$$

where κ_i^{o} is the bending rigidity of a patch of membrane o = +, − at lattice site i, and $\Delta_{\mathrm{d}} h_i^{\mathrm{o}}$ is the discretized Laplacian of the height field $\{h_i^{\mathrm{o}}\}$. We assume that $\kappa_i^{\mathrm{o}} = \kappa_{\mathrm{r}}^{\mathrm{o}}$ if the patch of membrane o at lattice site i contains a lipid raft, and $\kappa_i^{\mathrm{o}} = \kappa_{\mathrm{m}}^{\mathrm{o}}$ otherwise.

The membrane-anchored receptor (R) and ligand (L) proteins occupy single membrane patches and bind specifically to form R–L complexes with 1 : 1 stoichiometry. The spatial distribution of R's in the upper membrane is described by the composition field $\{m_i^+\}$ with values $m_i^+ = 0$ or 1 indicating the absence or presence of R at patch i. Likewise, $\{m_i^-\}$ with values $m_i^- = 0$ or 1 describes the spatial distribution of L's in the lower membrane. One R only binds one L if R and L are located at opposite membrane patches and their distance $l_i = h_i^+ - h_i^-$ is within the binding range, *i.e.*, $l_{\mathrm{c}} - l_{\mathrm{b}}/2 < l_i < l_{\mathrm{c}} + l_{\mathrm{b}}/2$, where l_{c} is the length of R–L complex and l_{b} is the width of the binding potential. The total energy of R–L complexes is[15,32,33,38]

$$\mathscr{H}_{\mathrm{R-L}} = -U_{\mathrm{b}} \sum_i m_i^+ m_i^- \theta\left(\frac{l_{\mathrm{b}}}{2} - |l_i - l_{\mathrm{c}}|\right) \quad (2)$$

where $\theta(\cdots)$ is the Heaviside's step function. We assume that l_{b}= 1 nm, l_{c}= 15 nm,[15,38] and the binding energy U_{b} is in the range of 3 to 6 $k_{\mathrm{B}}T$.[39,40]

The spatial distribution of lipid rafts is described by the composition fields $\{n_i^+\}$ and $\{n_i^-\}$ with values $n_i^{\mathrm{o}} = 0$ or 1 indicating, respectively, the absence or presence of lipid rafts in membrane o = +, − at lattice site i. The association of adhesion proteins with lipid rafts is taken into account by the coupling energy[39,41]

$$\mathscr{H}_{\mathrm{r-p}} = -U_{\mathrm{a}} \sum_i \left(n_i^+ m_i^+ + n_i^- m_i^-\right) \quad (3)$$

If R or L is moved from the membrane matrix to a lipid raft, the energy of the system decreases by U_{a}, which captures the affinity of R's and L's for lipid rafts. The raft-protein association energy U_{a} is chosen to be between 3 and $4k_{\mathrm{B}}T$ so that the protein concentration within lipid rafts is in the experimental range of around 10^3 to 10^4 $\mu\mathrm{m}^{-2}$.[42]

By analogy to the 2D lattice-gas model, the propensity of lipid rafts to coalesce is captured by a contact energy U between the nearest-neighbor raft patches. The total raft-raft contact energy is then[41]

$$\mathscr{H}_{\mathrm{r-r}} = -U \sum_{\langle i,j \rangle} \left(n_i^+ n_j^+ + n_i^- n_j^-\right) \quad (4)$$

where the sum runs over all pairs of nearest-neighbor patches $\langle i,j \rangle$. This short-ranged attraction ($U > 0$) drives the formation of raft domains, whereas the entropy of the lattice-gas-type system favors homogeneous states with many separate rafts.

The values of interaction parameters that enter eqn (2) and (3) are based on available experimental data and earlier computational studies.[15,38–40,42] In contrast, the contact energy U that enters eqn (4) is a variable in our model, which is varied systematically in our numerical calculations and simulations from 0 to U_0^*, where U_0^* is the contact energy of the 2D lattice-gas model at the critical point.

The Hamiltonian of the membrane system, $\mathscr{H}_{\mathrm{ad}} = \mathscr{H}_{\mathrm{me}} + \mathscr{H}_{\mathrm{R-L}} + \mathscr{H}_{\mathrm{r-p}} + \mathscr{H}_{\mathrm{r-r}}$, is a sum of the energy contributions given by eqn (1)–(4). The lattice spacing is taken to be a = 10 nm to match the average exclusion radius of membrane proteins.[43] Without loss of generality, we assume a symmetry of the two membranes, *i.e.*, (i) the area concentration of R's in the upper membrane is equal to the area concentration of L's in the lower membrane, $c_{\mathrm{p}} = \sum_i m_i^+/a^2 = \sum_i m_i^-/a^2$; (ii) the area fraction of raft patches is the same for the upper and lower membrane, $x = \sum_i n_i^+/N = \sum_i n_i^-/N$, where N is the total number of patches in each membrane; (iii) the two membranes have the same bending rigidities $\kappa_{\mathrm{r}} = \kappa_{\mathrm{r}}{}^+ = \kappa_{\mathrm{r}}{}^-$ of the raft patches and $\kappa_{\mathrm{m}} = \kappa_{\mathrm{m}}{}^+ = \kappa_{\mathrm{m}}{}^-$ of the membrane matrices. In our Monte Carlo (MC) simulations and mean field (MF) theory, c_{p} is varied between 0 and $0.2a^{-2}$, which corresponds to a maximal concentration of 2000 $\mu\mathrm{m}^{-2}$;[9] x is varied up to 0.3;[44] and κ_{m} attains the typical value of $10k_{\mathrm{B}}T$.[9,39,40]

We employed the MC method with the standard Metropolis criterion to explore the equilibrium properties of the membrane system. The system configuration was evolved *via* three types of trial moves: (i) vertical displacements of membrane patches to capture thermally-excited shape fluctuations of the membranes, (ii) lateral translations of R's and L's to mimic their diffusion, and (iii) lateral translations of raft patches. To prevent the two membranes from overlapping, trial moves of type (i) leading to $l_i < 0$ were rejected. The trial moves of type (i) led to variations in $\mathscr{H}_{\mathrm{me}}$ and $\mathscr{H}_{\mathrm{R-L}}$, type (ii) in $\mathscr{H}_{\mathrm{R-L}}$ and $\mathscr{H}_{\mathrm{r-p}}$, and type (iii) in $\mathscr{H}_{\mathrm{me}}$, $\mathscr{H}_{\mathrm{r-r}}$ and $\mathscr{H}_{\mathrm{r-p}}$. The proportion of these trial moves in each MC sweep (MCS) was chosen according to the physical timescales as in our earlier work.[39]

We performed the MC simulations in the canonical ensemble, *i.e.*, the number N of membrane patches, the protein concentration c_{p}, and the fraction x of raft patches were fixed in single simulation runs. We applied periodic boundary conditions in the x- and y-directions and simulated membranes with a size of up to $N = 100 \times 100$ patches, which corresponds the membrane area of 1 $\mu\mathrm{m}^2$. In each of the MC simulations, a relaxation run of 5×10^7 MCS was performed for thermal equilibration and a subsequent run of 5×10^7 MCS for statistical sampling. The simulation parameters were chosen according to existing literature data as specified in preceding paragraphs. To reveal the influence of membrane shape fluctuations and of bending rigidity contrast between the membrane matrix and lipid rafts, we considered two types of adhering membrane systems: (a) infinitely rigid and planar membranes with $\kappa_{\mathrm{r}} = \kappa_{\mathrm{m}} = \infty$ and $l_i = l_{\mathrm{c}}$ at any lattice site i; (b) flexible and fluctuating membranes with different values of the bending rigidity modulus, *i.e.*, $\kappa_{\mathrm{r}} = \kappa_{\mathrm{m}} = 10k_{\mathrm{B}}T$, $\kappa_{\mathrm{r}} = 3\kappa_{\mathrm{m}} = 30k_{\mathrm{B}}T$, and $\kappa_{\mathrm{r}} = 5\kappa_{\mathrm{m}} = 50k_{\mathrm{B}}T$. In the MC simulations of planar membranes, the trial moves of type (i) were omitted in order to totally suppress the membrane shape fluctuations.

To identify phase transitions in the membrane system, we monitored how the heat capacity per lattice site, $C_{\mathrm{V}} = (\langle \mathscr{H}_{\mathrm{ad}}{}^2 \rangle - \langle \mathscr{H}_{\mathrm{ad}} \rangle^2)/(Nk_{\mathrm{B}}T^2)$, was changing when the model parameters were

varied. The angular brackets $\langle \ldots \rangle$ denote the ensemble average. We also measured the R–L binding constant $K = [RL]/([R][L])$ by simply computing the area concentration [RL] of the R–L complexes, [R] of free R's, and [L] of free L's in the simulations.

We also used the mean field theory to explore the phase behavior of the system under study. The mean field calculation can be summarized as follows. Firstly, we introduce a grand-canonical Hamiltonian, as given by eqn (S1) in the ESI,† and perform all subsequent calculations in the grand-canonical ensemble. Secondly, we apply the mean filed approximation to the composition fields $\{n_i^+\}$ and $\{n_i^-\}$. Thirdly, by integrating out the degrees of freedom of R's and L's in the grand-canonical partition function, we map the model defined by eqn (1)–(4) onto a model of two homogeneous membranes interacting *via* an effective potential as described by eqn (S5) and (S6) in the ESI.† Fourthly, we derive a self-consistent equation for free-energy minima, see eqn (S9) in the ESI.† Next, we use MC simulations to determine the contact probability P_b of the homogeneous membranes, which is a quantity that enters eqn (S9) (ESI†). In the case of planar membranes, we set $P_b = 1$. Finally, we solve the self-consistent equation numerically to identify phase transition points and critical points.

3 Results and discussion

3.1 Receptor–ligand binding induces formation of membrane domains

Monte Carlo simulations of the lattice model show that for relatively small contact energies, U, the system is homogeneous with many small rafts distributed more-or-less uniformly in the membranes (Fig. 1b), whereas at sufficiently large values of U the system is phase separated with rafts forming stable mesoscale domains (Fig. 1c). To explore the phase behavior of the system, it is constructive to consider first a limiting case of planar and infinitely rigid membranes ($\kappa_r = \kappa_m = \infty$) without R's and L's ($c_p = 0$). In this limit, the membrane model reduces to the 2D lattice-gas model whose phase behavior is described by the exact solution of the 2D Ising model on the square lattice.[45] The phase separation can take place only above the critical point, *i.e.*, at $U > U_0^*$, where the critical contact energy $U_0^* = 2\ln(1+\sqrt{2})k_BT$. Within the MF theory, however, $U_0^* = k_BT$.

The flexibility of the adhering membranes as well as the presence of the R's and L's that associate with lipid rafts modify the phase behavior of the system. Fig. 2a–c show MC simulation results for three membrane systems with different bending rigidities κ_r and κ_m. In each of the three systems, the area concentration of adhesion proteins $c_p = 500\ \mu m^{-2}$, the fraction of raft patches $x = 0.2$, the R–L binding energy $U_b = 6k_BT$, and the protein-raft association energy $U_a = 3k_BT$. The triangles show the heat capacity per lattice site, C_V, as a function of contact energy U. We identify the maxima in the C_V *versus* U plots with phase transition points (vertical dashed lines). Importantly, the transitions from homogeneous to separated phases occur in each of the three system at contact energies $U < U_0^*$, which indicates that the adhesion of membranes induces phase separation. The dots show the binding constant, K, as a function of U. Interestingly, K increases abruptly in the

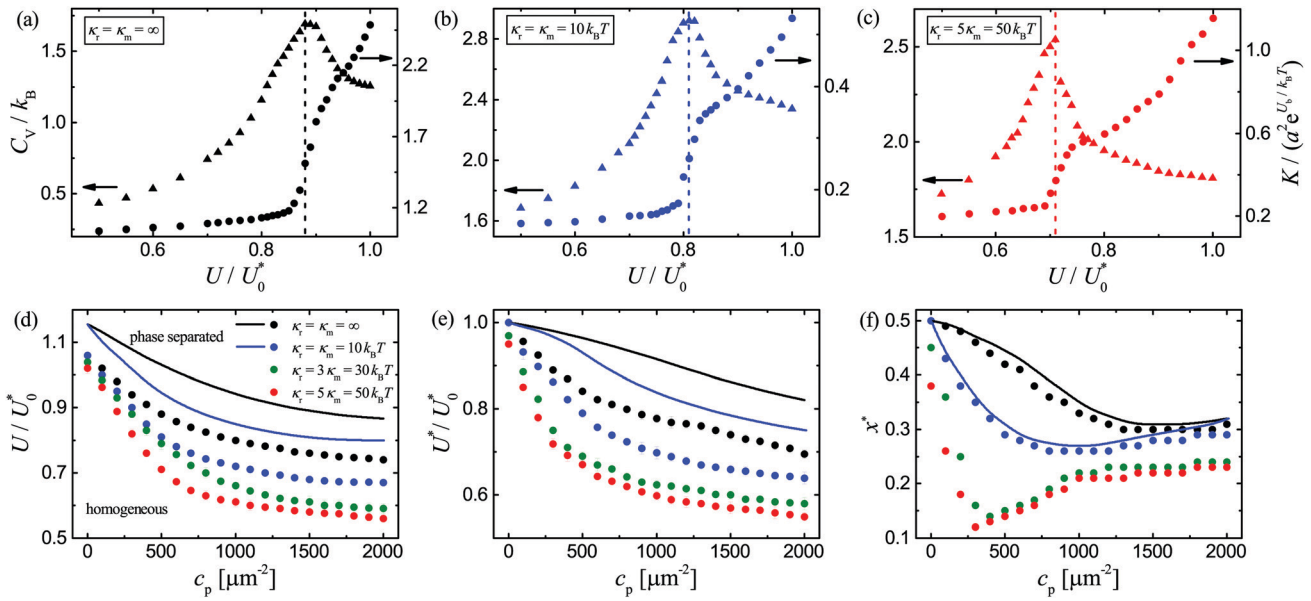

Fig. 2 Phase behavior of the adhering membranes with the R–L binding energy $U_b = 6k_BT$ and the protein-raft association energy $U_a = 3k_BT$. Bending rigidities of the membrane matrix κ_m and lipid rafts κ_r are specified in each panel. (a)–(c) Heat capacity C_V (triangles) and binding constant K (dots) *versus* contact energy U as obtained from MC simulations with protein concentration $c_p = 500\ \mu m^{-2}$ and raft area fraction $x = 0.2$. The vertical dashed lines indicate the location of maximum C_V, which determines the phase transition points. (d) Phase diagram in the (c_p, U) coordinates for $x = 0.2$. The regimes corresponding to the homogeneous and phase-separated membrane states are indicated. The dots indicate the phase transition points determined in the MC simulations from the C_V *versus* U plots as in panels (a)–(c). The lines show the MF calculation results. (e) Critical contact energy U^* and (f) critical raft area fraction x^* *versus* c_p. The lines show predictions of the MF theory and the dots indicate the MC simulation results. The color code is as in panel (d).

vicinity of the phase transition points, implying an interplay between the R–L binding and the phase transition.

3.2 Flexibility of membranes and rigidity of lipid rafts facilitate the formation of membrane domains

The simulation data in Fig. 2a–c show that the phase transition point shifts from $U = 0.88U_0^*$ for infinitely rigid membranes ($\kappa_r = \kappa_m = \infty$, Fig. 2a) to $U = 0.81U_0^*$ for flexible membranes with uniform bending rigidity ($\kappa_r = \kappa_m = 10k_BT$, Fig. 2b) to $U = 0.71U_0^*$ for flexible membranes with bending rigidity contrast between the membrane matrix and lipid rafts ($\kappa_r = 5\kappa_m = 50k_BT$, Fig. 2c). These results indicate that the R–L binding together with the association of R's and L's with lipid rafts shift the phase transition point below U_0^*. Membrane fluctuations and an increased rigidity of lipid rafts further decrease the value of contact energy U at which the phase transition occurs.

In the case of flexible membranes, the formation of R–L complexes suppresses membrane fluctuations and induces an effective, membrane-mediated, lateral attraction between the R–L complexes.[16,46,47] This lateral attraction acting between the raft-associated R–L complexes promotes coalescence of lipid rafts.[41] In the case of planar and infinitely rigid membranes, in contrast, the formation of R–L complexes obviously does not impose any restrictions on membrane conformations and, thus, there is no membrane-mediated, lateral attraction between the raft-associated R–L complexes. Therefore, phase separation in the fluctuating membrane system (Fig. 2b) can take place at smaller contact energies U than in the planar membrane system (Fig. 2a). Membrane fluctuations induce also long-ranged attraction between lipid rafts that are more rigid than the membrane matrix.[48–50] These fluctuation-induced attractive interactions give rise to clustering and coalescence of lipid rafts, which explains why the bending rigidity contrast, $\kappa_r > \kappa_m$, facilitates the phase separation (Fig. 2c).

To explore the phase behavior further, we performed systematic MC simulations with c_p ranging from 0 to 2000 μm^{-2}, U/U_0^* between 0.4 and 1.2, and x in the range from 0 to 0.3. We identified the phase transitions based on the C_v *versus* U plots, as illustrated in Fig. 2a–c. The resulting phase diagrams in the (c_p, U) coordinates for $x = 0.2$, $U_b = 6k_BT$ and $U_a = 3k_BT$ are shown in Fig. 2d. By comparing the results obtained for infinitely rigid membranes ($\kappa_r = \kappa_m = \infty$; black dots) and flexible membranes ($\kappa_r = \kappa_m = 10k_BT$; blue dots) we conclude that membrane flexibility and fluctuations lower the values of U at which the phase transitions occur. This effect is qualitatively confirmed by the MF calculations (black and blue lines). For the sake of comparing the MC and MF phase diagrams in Fig. 2d, we rescale U by $U_0^* = 2\ln(1+\sqrt{2})k_BT$ for the MC data and by $U_0^* = k_BT$ for the MF results. Analogous phase diagrams for other values of x, U_b and U_a are shown in Fig. S3a–c and S4a–c (ESI†).

It can be also seen in Fig. 2d that as the rigidity of lipid rafts increases from $\kappa_r = \kappa_m = 10k_BT$ (blue dots) to $\kappa_r = 3\kappa_m = 30k_BT$ (green dots) to $\kappa_r = 5\kappa_m = 50k_BT$ (red dots), the phase transitions take place at successively smaller values of contact energy U. This tendency is observed over a range of parameters c_p and x examined in the MC simulations (phase diagrams for other values of x, U_b and U_a are displayed in Figs. S1, S3a–c and S4a–c, ESI†). Therefore, the R–L binding together with the contrast between κ_r and κ_m facilitate the coalescence of lipid rafts into mesoscopic domains.

In addition to the phase diagrams in the (c_p, U) coordinates (Fig. 2d and Fig. S1a–b, S3a–c, S4a–c, ESI†), we also constructed phase diagrams in the (x, U) coordinates (an example is shown in Fig. S2, ESI†) where we found two lines of transition points meeting at the critical point (x^*,U^*). The phase diagrams in the (x, U) coordinates are in fact analogous to classical binary mixture phase diagrams in the coordinates of mole fraction and inverse temperature. We determined the critical points (x^*,U^*) for protein concentrations c_p ranging up to 2000 μm^2 and for different rigidities κ_r and κ_m. Fig. 2e and f show, respectively, U^* and x^* as functions of c_p for $U_b = 6k_BT$, $U_a = 3k_BT$ and different rigidities κ_r and κ_m. Analogous dependencies of U^* on c_p for other values of U_b and U_a are shown in Figs. S3d and S4d (ESI†). The results of MC simulations (dots) show that U^* decreases with c_p and that U^* can be reduced by up to $\sim$50% relative to U_0^* for flexible membranes with a substantial contrast between κ_r and κ_m (red dots). The MF theory (solid lines) gives the right trend but underestimates the reduction in U^* because it does not fully accounts for thermal fluctuations in the membrane system. The dependence of x^* on c_p is non-monotonic and x^* can be much smaller than 0.5 due to the R–L binding (Fig. 2f). For infinitely rigid membranes ($\kappa_r = \kappa_m = \infty$) and flexible membranes with no bending rigidity contrast ($\kappa_r = \kappa_m = 10k_BT$), the MF results are in good agreement with the MC simulations. The results presented in Fig. 2e and f indicate that, in a biologically relevant range of parameters, changes in protein concentration or lipid composition can bring the system to criticality.

3.3 Association of adhesion proteins with lipid rafts increases both affinity and cooperativity of the receptor–ligand binding

As indicated already in Fig. 2a–c, the binding constant K increases abruptly when the membrane system undergoes the phase transition. We performed extensive MC simulations to explore how K depends on U for various choices of parameters x, U_a, U_b, κ_r and κ_m. The simulation results are presented in Fig. 3 and Fig. S5, S6 (ESI†). They all show clearly that the rapid increase in K coincides with the phase transition, regardless of the specific values of model parameters. The binding constant K therefore represents a general indicator of the phase transition in the system under study. Moreover, the rapid increase in K indicates cooperativity of the R–L binding.

To quantify the R–L binding cooperativity, we produced the Hill plots by varying the area concentration c_p of R's and L's up to 2000 μm^{-2}. Fig. 4 shows the plots of log([RL]/[R]) *versus* log([L]) for $U_b = 6k_BT$, $U_a = 3k_BT$ and different values of raft fraction x, contact energy U and bending rigidities κ_r and κ_m. The resulting values of the Hill coefficient n_H for each data set are indicated in Fig. 4. A reference line is provided by the Hill plot for infinitely rigid and planar membranes without lipid

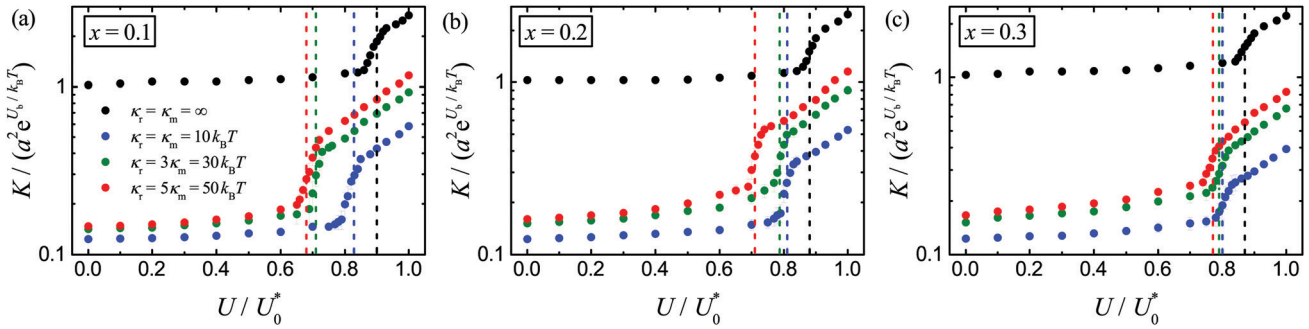

Fig. 3 Binding constant K as a function of contact energy U as obtained from MC simulations with $U_b = 6k_BT$, $U_a = 3k_BT$, $c_p = 500\ \mu m^{-2}$, and $x = 0.1$ (a), 0.2 (b), and 0.3 (c). Different colors correspond to different combinations of bending rigidities κ_r and κ_m, as specified in panel (a). The vertical dashed lines in different colors indicate the locations of maximum C_V, as in Fig. 2a–c, for the corresponding membrane systems.

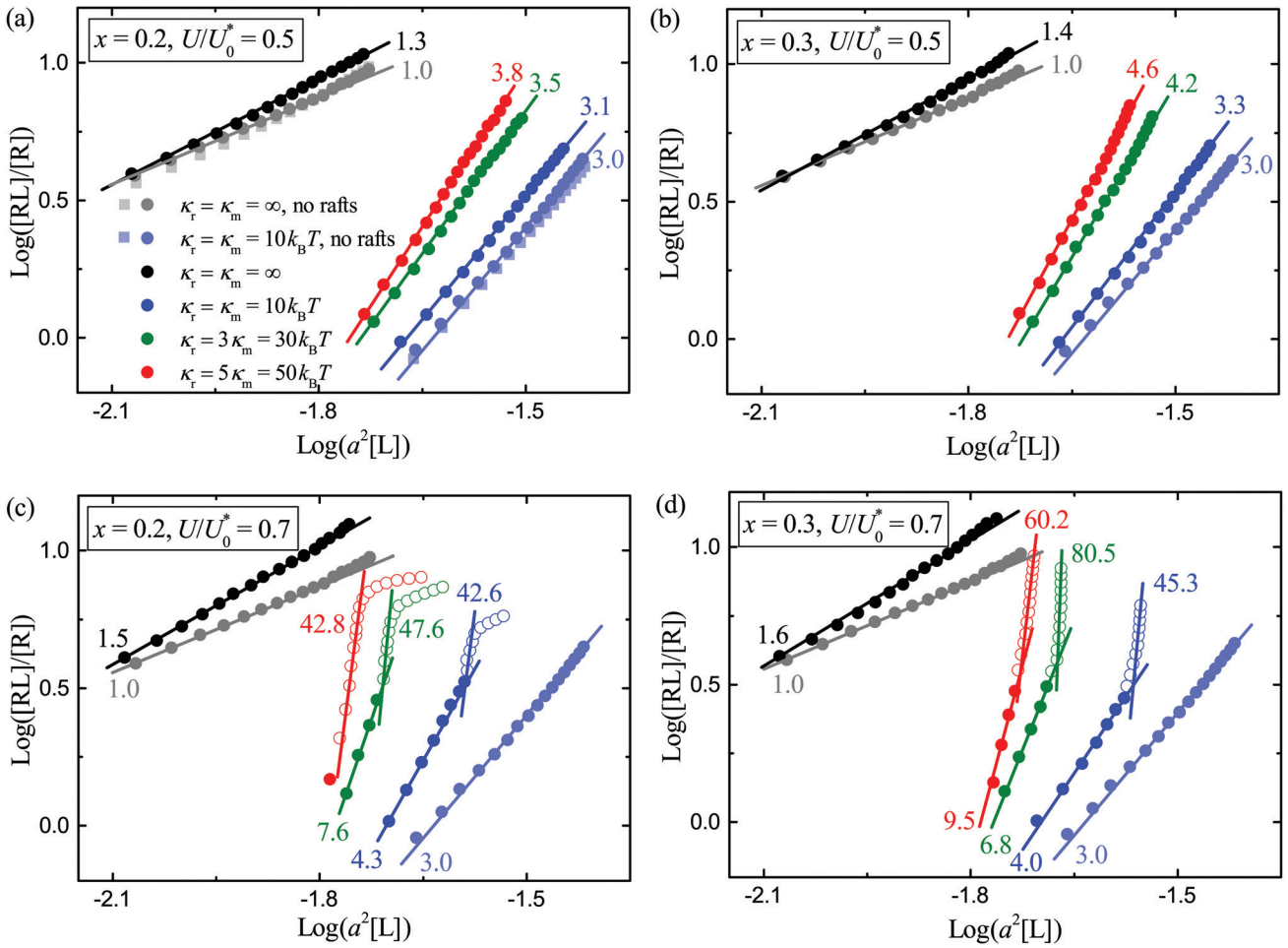

Fig. 4 Hill plots for the R–L binding. The contact energy U and area fraction x of lipid rafts are indicated in each panel. The data points marked as dots and squares were obtained, respectively, from MC simulations and MF calculations with $U_b = 6k_BT$ and $U_a = 3k_BT$. The different colors indicate different combinations of bending rigidities κ_r and κ_m, as denoted in panel (a). The filled and open dots correspond to homogeneous and phase-separated membranes, respectively. Solid lines represent linear fits to the MC data points; their slopes are indicated and equal to the values of the Hill coefficient n_H.

rafts (gray points). In this limiting case ($\kappa_r = \kappa_m = \infty$ and $x = 0$), both the MF theory (gray squares) and the MC simulations (gray dots) yield $n_H = 1$, which means no binding cooperativity, as expected. Another reference line is provided by the Hill plot for flexible membranes without lipid rafts (light blue points). In this special case ($\kappa_r = \kappa_m = 10k_BT$ and $x = 0$), both the MF theory (light blue squares) and the MC simulations (light blue dots) lead to $n_H = 3$, consistent with the modified law of mass action

$[RL] \propto [R]^2[L]^2$ for the binding of R's and L's anchored to flexible and homogeneous membranes.[9,15] Indeed, since the total number of R's is equal to the total number of L's in the MC simulations, and R's bind L's in 1 : 1 stoichiometry, the area concentrations of free R's and free L's are equal, [R] = [L]. The modified law of mass action, $[RL] \propto [R]^2[L]^2$, implies then $[RL]/[R] \propto [L]^3$, leading to $n_H = 3$.

The presence of lipid rafts ($x > 0$ and $U > 0$) results in an increase of the Hill coefficient (gray *versus* black points and light blue *versus* dark blue points in Fig. 4). At $U = 0.5U_0^*$, no phase separation occurs in the system (Fig. 2d) and the values of n_H remain constant as [L] is varied at fixed values of x, κ_r and κ_m (Fig. 4a and b). For infinitely rigid membranes (black dots), the values of n_H remain close to 1 as the area fraction of lipid raft is increased up to $x = 0.3$. However, for flexible membranes (red, green and dark blue dots), n_H takes values larger than 3 and increases with x. Moreover, increasing the bending rigidity of lipid rafts from $\kappa_r = \kappa_m = 10k_BT$ (blue dots) to $\kappa_r = 3\kappa_m = 30k_BT$ (green dots) to $\kappa_r = 5\kappa_m = 50k_BT$ (red dots) leads to successive increase of n_H. Taken together, these results indicate that colocalization of R's and L's with lipid rafts facilitates the formation of additional R–L complexes around the ones already formed, whereas the effective, membrane-mediated attraction between rigid rafts with $\kappa_r > \kappa_m$ further enhances the R–L binding cooperativity.

At $U = 0.7U_0^*$, the phase separation can occur if the area concentration of R's and L's is sufficiently large (Fig. 2d). As shown in Fig. 4c and d, the transitions from homogeneous (filled dots) to separated (open dots) phases involve about one order-of-magnitude increase in n_H. To rule out finite size effects, we performed MC simulations of smaller membranes with 60×60 lattice sites and obtained identical results (Fig. S7, ESI†). The decrease in the slope for the last few data points in Fig. 4c (red, green and dark blue) arises from the fact that, at small fractions x and large concentrations c_p, the rafts cannot accommodate more proteins, leading to a decrease in K as illustrated in Fig. S8 (ESI†).

4 Conclusions

We performed MC simulations and MF calculations to explore collective and cooperative phenomena in systems of adhering membranes in which the receptor (R) and ligand (L) proteins have affinity for lipid rafts (Fig. 1). Our results show that the R–L binding can induce coalescence of lipid rafts into mesoscale domains (Fig. 1c). The mechanism for the formation of these membrane domains involves collective, fluctuation-induced, membrane-mediated interactions between the R–L complexes. We quantified how the domain formation is influenced by different physical properties of the membrane system, including (i) flexibility of the membranes, (ii) propensity of lipid rafts to coalesce, (iii) the amount of lipid rafts in the membranes, (iv) the area concentration of R's and L's, (v) the strength of R–L binding, and (vi) the affinity of the R's and L's for lipid rafts (Fig. 2 and Fig. S1–S4, ESI†). Our results reveal that a key factor that facilitates the domain formation is the contrast in bending rigidities between the membrane matrix and lipid rafts.

Our results show also that the affinity of R–L binding increases dramatically when phase separation occurs in the system (Fig. 2a–c, 3 and Fig. S5, S6, ESI†). This effect can be explained as follows. When lipid rafts coalesce into mesoscopic domains, the area concentration of R's and L's in these domains is significantly larger than in the homogeneous membranes prior to the domain formation. This effective increase in concentrations of R's and L's amplifies the R–L binding rate, which in turn elevates the apparent binding constant. In addition, aggregation of R's and L's in the domains smoothens out the membranes locally, which facilitates the cooperative binding of the adhesion receptors to their ligands. Importantly, the amplification of binding affinity caused by the aggregation of R's and L's within the raft-type domains is consistent with experimental observations, namely, that lipid rafts control the desmosome assembly and the strength of cell adhesion,[51] and that the lateral organization of lipids in endothelial cell membranes modulates integrin adhesion, nascent adhesion formation, and cell migration.[52]

The results of MC simulations show also that the cooperativity of R–L binding is increased by association of R's and L's with lipid rafts (Fig. 4 and Fig. S7, ESI†). The cooperativity of R–L binding results from three distinct processes: (i) association of R's and L's with lipid rafts exhibiting propensity for coalescence, (ii) fluctuation-induced, long-ranged, attractive interactions between lipid rafts with bending rigidity κ_r larger than rigidity κ_m of the membrane matrix,[48–50] and (iii) suppression of membrane fluctuations due to the formation of R–L complexes, which facilitates the R–L binding.[9,10,15] The former process is predominant when lipid rafts form mesoscale domains, which coincides with aggregation of R's and L's within these domains. The cooperativity of R–L binding is then most significant, as indicated by large values of the Hill coefficient ranging up to 80 in the MC simulations (Fig. 4).

The observed interplay between the formation of mesoscale membrane domains and the amplification of the affinity and cooperativity of the R–L binding displays acute sensitivity of the membrane system to changes in such parameters as the amount of raft-favoring lipids in the membranes or the concentration of adhesion receptors, which can be actively tuned in diverse cellular processes. Our studies quantify how the collective and cooperative phenomena occurring in the model system depend on the bending rigidities of the membrane matrix and lipid rafts, which gives us a hint on how intercellular contacts can be influenced by the flexibility of cell membranes, which can be modulated by such microenvironmental factors as the acidity of tumors.[10]

The mesoscale model used in this study takes into account several generic features of cell membranes. However, it cannot capture molecular properties of specific receptor and ligand proteins, which is a relevant limitation of the current study. To overcome this limitation in future studies, one may use a multi-scale approach in which a specific receptor–ligand complex is simulated in molecular details and the resulting data are taken as input to simulations of the mesoscale model.[10]

Another limitation of the lattice model is an underlying assumption that the total area of lipid rafts is a fixed quantity. We note that this assumption does not have to be fulfilled exactly when lipid rafts coalesce to form mesoscopic domains upon membrane adhesion. This limitation of the lattice model obviously does not pertain to molecular dynamics simulations which, however, would be extremely time-consuming and challenging when used to explore adhesion of micrometer-size membranes as studied here.

Author contributions

J. H., B. R. and F. S. designed the research project; L. L. performed computer simulations and analytical calculations; J. H. supervised the computer simulations; J. H. and B. R. provided advice on the analytical calculations; L. L., J. H., X. S., B. R. and F. S. analyzed and interpreted the results; L. L., J. H. and B. R. wrote the manuscript.

Conflicts of interest

There are no conflicts to declare.

Acknowledgements

L. Li, J. Hu and F. Song acknowledge support from the Programs in the National Key Research and Development Program of China (Grant No. 2016YFA0501601), the National Natural Science Foundation of China (Grants No. 21973040, 21504038, 11902327 and 11972041), the Strategic Priority Research Program of the Chinese Academy of Sciences (Grant No. XDB22040102), and Opening Fund of State Key Laboratory of Nonlinear Mechanics. J. Hu also acknowledges support from the Fundamental Research Funds for the Central Universities (Grant No. 14380228). B. Różycki acknowledges support from the National Science Centre, Poland, Grant No. 2016/21/B/NZ1/00006. The numerical calculations were performed on the computing facilities in the High Performance Computing Center (HPCC) of Nanjing University.

Notes and references

1 J. B. Huppa, M. Axmann, M. A. Mörtelmaier, B. F. Lillemeier, E. W. Newell, M. Brameshuber, L. O. Klein, G. J. Schütz and M. M. Davis, *Nature*, 2010, **463**, 963–967.
2 J. Huang, V. I. Zarnitsyna, B. Liu, L. J. Edwards, N. Jiang, B. D. Evavold and C. Zhu, *Nature*, 2010, **464**, 932–936.
3 G. P. O'Donoghue, R. M. Pielak, A. A. Smoligovets, J. J. Lin and J. T. Groves, *eLife*, 2013, **2**, e00778.
4 B. Liu, W. Chen, B. D. Evavold and C. Zhu, *Cell*, 2014, **157**, 357–368.
5 Q. Li, A. Wayman, J. Lin, Y. Fang, C. Zhu and J. Wu, *Biophys. J.*, 2016, **111**, 686–699.
6 L. Limozin, P. Bongrand and P. Robert, *Sci. Rep.*, 2016, **6**, 35193.
7 Y. Chen, L. A. Ju, F. Zhou, J. Liao, L. Xue, Q. P. Su, D. Jin, Y. Yuan, H. Lu, S. P. Jackson and C. Zhu, *Nat. Mater.*, 2019, **18**, 760–769.
8 C. Zhu, W. Chen, J. Lou, W. Rittase and K. Li, *Nat. Immunol.*, 2016, **20**, 1269–1278.
9 J. Hu, R. Lipowsky and T. R. Weikl, *Proc. Natl. Acad. Sci. U. S. A.*, 2013, **110**, 15283–15288.
10 J. Steinkühler, B. Różycki, C. Alvey, R. Lipowsky, T. R. Weikl, R. Dimova and D. E. Discher, *J. Cell Sci.*, 2019, **132**, jcs216770.
11 A. Tolosa-Diaz, V. G. Almendro-Vedia, P. Natale and I. Lopez-Montero, *Biomolecules*, 2020, **10**, 1085.
12 V. Junghans, M. Chouliara, A. M. Santos, D. Hatherley, J. Petersen, T. Dam, L. M. Svensson, J. Rossjohn, S. J. Davis and P. Jönsson, *J. Cell Sci.*, 2020, **133**, jcs245985.
13 J. Monod, J. Wyman and J. P. Changeux, *J. Mol. Biol.*, 1965, **12**, 88–118.
14 T. S. Teo and J. H. Wang, *J. Biol. Chem.*, 1973, **248**, 5950–5955.
15 H. Krobath, B. Różycki, R. Lipowsky and T. R. Weikl, *Soft Matter*, 2009, **5**, 3354–3361.
16 T. R. Weikl, M. Asfaw, H. Krobath, B. Różycki and R. Lipowsky, *Soft Matter*, 2009, **5**, 3213–3224.
17 G. K. Xu, J. Hu, R. Lipowsky and T. R. Weikl, *J. Chem. Phys.*, 2015, **143**, 243137.
18 J. Hu, G. K. Xu, R. Lipowsky and T. R. Weikl, *J. Chem. Phys.*, 2015, **143**, 243136.
19 D. Lingwood and K. Simons, *Science*, 2010, **327**, 46–50.
20 I. Levental and S. L. Veatch, *J. Mol. Biol.*, 2016, **428**, 4749–4764.
21 E. Sezgin, I. Levental, S. Mayor and C. Eggeling, *Nat. Rev. Mol. Cell Biol.*, 2017, **18**, 361–374.
22 I. Levental, K. R. Levental and F. A. Heberle, *Trends Cell Biol.*, 2020, **30**, 341–353.
23 X. Q. Lin, X. B. Lin and N. Gu, *Nanoscale*, 2020, **12**, 4101–4109.
24 F. Perissinotto, C. Stani, E. D. Cecco, L. Vaccari, V. Rondelli, P. Posocco, P. Parisse, D. Scaini, G. Legname and L. Casalis, *Nanoscale*, 2020, **12**, 7631–7640.
25 J. H. Lorent, B. Diaz-Rohrer, X. Lin, K. Spring, A. A. Gorfe, K. R. Levental and I. Levental, *Nat. Commun.*, 2017, **8**, 1219.
26 H. A. Anderson, E. M. Hiltbold and P. A. Roche, *Nat. Immunol.*, 2020, **1**, 156–162.
27 T. Murai, C. Sato, M. Sato, H. Nishiyama, M. Suga, K. Mio and H. Kawashima, *J. Cell Sci.*, 2013, **126**, 3284–3294.
28 H. A. Anderson and P. A. Roche, *Biochim. Biophys. Acta, Mol. Cell Res.*, 2015, **1853**, 775–780.
29 B. Shao, T. Yago, H. Setiadi, Y. Wang, P. Mehta-D'souza, J. Fu, P. R. Crocker, W. Rodgers, L. Xia and R. P. McEver, *Proc. Natl. Acad. Sci. U. S. A.*, 2015, **112**, 8661–8666.
30 X. Su, J. A. Ditlev, E. Hui, W. Xing, S. Banjade, J. Okrut, D. S. King, J. Taunton, M. K. Rosen and R. D. Vale, *Science*, 2016, **352**, 595–599.
31 M. B. Stone, S. A. Shelby, M. F. Nunez, K. Wisser and S. L. Veatch, *eLife*, 2017, **6**, e19891.
32 T. R. Weikl and R. Lipowsky, *Phys. Rev. E: Stat., Nonlinear, Soft Matter Phys.*, 2001, **64**, 011903.

33 M. Asfaw, B. Rożycki, R. Lipowsky and T. R. Weikl, *Europhys. Lett.*, 2006, **76**, 703–709.
34 L. Li, X. Wang, Y. Shao, W. Li and F. Song, *Sci. China: Phys., Mech. Astron.*, 2018, **61**, 128711.
35 H. Noguchi and G. Gompper, *Proc. Natl. Acad. Sci. U. S. A.*, 2005, **102**, 14159–14164.
36 A. H. Bahrami and T. R. Weikl, *Nano Lett.*, 2018, **18**, 1259–1263.
37 W. Helfrich, *Z. Naturforsch., C: J. Biosci.*, 1973, **28**, 693–703.
38 B. Różycki, R. Lipowsky and T. R. Weikl, *New J. Phys.*, 2010, **12**, 095003.
39 L. Li, J. Hu, X. Shi, Y. Shao and F. Song, *Soft Matter*, 2017, **13**, 4294–4304.
40 L. Li, J. Hu, G. Xu and F. Song, *Phys. Rev. E*, 2018, **97**, 012405.
41 L. Li, J. Hu, B. Różycki and F. Song, *Nano Lett.*, 2020, **20**, 722–728.
42 K. Simons and D. Toomre, *Nat. Rev. Mol. Cell Biol.*, 2000, **1**, 31–39.
43 P. K. Tsourkas, M. L. Longo and S. Raychaudhuri, *Biophys. J.*, 2008, **95**, 1118–1125.
44 M. Fallahi-Sichani and J. J. Linderman, *PLoS One*, 2009, **4**, e6604.
45 E. W. Montroll, R. B. Potts and J. C. Ward, *J. Math. Phys.*, 1963, **4**, 308–322.
46 T. Speck, E. Reister and U. Seifert, *Phys. Rev. E: Stat., Nonlinear, Soft Matter Phys.*, 2010, **82**, 021923.
47 S. F. Fenz, T. Bihr, D. Schmidt, R. Merkel, U. Seifert, K. Sengupta and A. S. Smith, *Nat. Phys.*, 2017, **13**, 906–913.
48 R. R. Netz and P. Pincus, *Phys. Rev. E: Stat., Nonlinear, Soft Matter Phys.*, 1995, **52**, 4114–4128.
49 D. S. Dean and M. Manghi, *Phys. Rev. E: Stat., Nonlinear, Soft Matter Phys.*, 2006, **74**, 021916.
50 J. Hu, T. Weikl and R. Lipowsky, *Soft Matter*, 2011, **7**, 6092–6102.
51 N. Resnik, K. Sepcic, A. Plemenitas, R. Windoffer, R. Leube and P. Veranic, *J. Biol. Chem.*, 2011, **286**, 1499–1507.
52 S. Son, G. J. Moroney and P. J. Butler, *Biophys. J.*, 2017, **113**, 1080–1092.

